ELSEVIER

Modelling of cells, stacks and systems based around metal-supported planar IT-SOFC cells with CGO electrolytes operating at 500–600 °C

R.T. Leah [a,*], N.P. Brandon [a,b], P. Aguiar [b]

[a] *Ceres Power Ltd., Unit 18, Denvale Trade Park, Haslett Avenue East, Crawley RH10 1SS, UK*
[b] *Department of Chemical Engineering and Chemical Technology, Imperial College London, London SW7 2AZ, UK*

Abstract

Ceres Power Ltd. has developed a novel solid oxide fuel cell (SOFC) concept based upon depositing a thick film positive–electrolyte–negative (PEN) structure on a porous stainless steel substrate, and using gadolinia-doped ceria (CGO) as the electrolyte material. This approach allows the temperature of operation to be reduced to below 600 °C, well below the conventional SOFC operating temperature. Historically, the use of CGO as an electrolyte material has been viewed as impractical because of its poor stability in reducing atmospheres at elevated temperatures, leading to electronic conductivity, which effectively short-circuits the cell leading to a loss of efficiency. In this work, a model is developed which accurately simulates the polarisation behaviour of a Ceres cell including electronic leakage. The parameters of this model are set to give the best possible fit to experimental data. This cell model is then incorporated into a model of a 2.5 kW$_e$ stack, and the stack model into a natural gas fuelled combined heat and power (CHP) system model. The system model demonstrates that high operating efficiencies are achievable for such a system based upon IT-SOFC cells with CGO electrolytes.
© 2005 Elsevier B.V. All rights reserved.

Keywords: Metal-supported IT-SOFC; CGO; Modelling; System efficiency; Electronic leakage current

1. Introduction

Solid-oxide fuel cells (SOFCs) are a promising technology for highly efficient power generation from both hydrogen and hydrocarbon fuels, particularly for small units where the efficiency of energy conversion exceeds that of other competing technologies. The operation of SOFCs relies on the ability of certain metal-oxide based ceramics to conduct oxide ions at elevated temperatures. These materials are used as the ion-conducting electrolyte of the fuel cell. The ceramic oxide material generally used is yttria stabilised zirconia (YSZ), which is a pure ionic conductor. The relatively low oxide ion conductivity of this material dictates that even in very thin-film form the minimum practical operating temperature of the fuel cell is around 650 °C, and more typically 700–900 °C. These high operating temperatures have generally caused problems in the construction

of cost-effective SOFC generators because of the high cost of materials for stack and system construction able to withstand such temperatures for the thousands of hours required for a practical system life. Traditional SOFC cells are all-ceramic devices, which also cause problems because of the mechanical fragility of ceramics, particularly when sealed to other ceramic or metal components in a stack. Ceres Power Ltd. has developed a novel SOFC cell technology based upon the use of a thick-film positive–electrolyte–negative (PEN) structure deposited on a ferritic stainless steel substrate, which provides the mechanical support for the cell. This technology has been described more fully by Brandon et al. [1].

Ceres SOFCs use cerium gadolinium oxide (CGO) instead of YSZ as the electrolyte material. CGO has a far higher ionic conductivity than YSZ, allowing practical fuel cell operation down to 500 °C if the electrolyte is in thick-film form (typically 10–15 μm thick). However, the use of CGO has historically been viewed as impractical because CGO is

Nomenclature

$D_{\text{eff,anode}}$ anode effective diffusivity ($m^2\,s^{-1}$)

$D_{\text{eff,cathode}}$ cathode effective diffusivity ($m^2\,s^{-1}$)

E_{AA} anode activation energy ($J\,mol^{-1}$)

E_{AC} cathode activation energy ($J\,mol^{-1}$)

F Faraday constant ($C\,mol^{-1}$)

$\Delta G^{\circ}_{\text{H}_2}$ Gibb's free energy of hydrogen combustion ($J\,mol^{-1}$)

j current density ($A\,m^{-2}$)

j_{E} electronic leakage current density in electrolyte ($A\,m^{-2}$)

j_{I} total current density in electrolyte ($A\,m^{-2}$)

j_{T} current density in external circuit ($A\,m^{-2}$)

$j_{0\text{A}}$ anode exchange current density ($A\,m^{-2}$)

$j_{0\text{C}}$ cathode exchange current density ($A\,m^{-2}$)

K_{A} anode pre-exponential factor ($S\,m^{-2}\,bar^{-0.5}$)

K_{C} cathode pre-exponential factor ($S\,m^{-2}$)

K_{I} ionic conductivity pre-exponential factor ($S\,K\,m^{-1}$)

n number of electrons transferred per mole of reactant

P operating pressure (bar)

$p^{\text{inter}}_{\text{H}_2}$ hydrogen partial pressure at electrolyte/anode interface (bar)

$p^{0}_{\text{H}_2}$ hydrogen partial pressure in bulk fuel stream (bar)

$p^{\text{inter}}_{\text{H}_2\text{O}}$ steam partial pressure at electrolyte/anode interface (bar)

$p^{0}_{\text{H}_2\text{O}}$ steam partial pressure in bulk fuel stream (bar)

$p^{\text{inter}}_{\text{O}_2}$ oxygen partial pressure at electrolyte/cathode interface (bar)

$p^{0}_{\text{O}_2}$ oxygen partial pressure in bulk air stream (bar)

$p_{\text{O}_2\text{local}}$ local oxygen partial pressure in the electrolyte (bar)

p^{θ} oxygen partial pressure at which ionic and electronic conductivity of CGO electrolyte are equal (bar)

R_{cont} area specific contact resistance ($\Omega\,m^2$)

R_{m} ideal gas constant ($J\,mol^{-1}\,K^{-1}$)

R_{ohm} ohmic area specific resistance ($\Omega\,m^2$)

r area specific rate of electrode reaction ($mol\,m^{-2}\,s^{-1}$)

T temperature (K)

V_0 theoretical open-circuit potential of hydrogen fuel cell (V)

$V_{0\text{C}}$ cathode potential (V)

V_{cell} cell terminal potential (V)

Greek letters

$\delta V^{\text{act}}_{\text{A}}$ anode activation overpotential (V)

$\delta V^{\text{act}}_{\text{C}}$ cathode activation overpotential (V)

σ_{anode} electronic conductivity of the anode ($S\,m^{-1}$)

σ_{cathode} electronic conductivity of the cathode ($S\,m^{-1}$)

σ_{ele} electronic conductivity of the electrolyte ($S\,m^{-1}$)

σ_{eli} ionic conductivity of the electrolyte ($S\,m^{-1}$)

τ_{el} thickness of the electrolyte (m)

τ_{anode} thickness of the anode (m)

τ_{cathode} thickness of the cathode (m)

$\tau_{\text{holepitch}}$ half distance between holes in the substrate (m)

$\tau_{\text{substrate}}$ thickness of the metal substrate (m)

less chemically stable than YSZ, undergoing reduction in the conditions typically experienced in the fuel compartment of an SOFC [2]. This reduction leads to the CGO exhibiting some mixed ionic/electronic conductivity, which leads to an internal short-circuit in the cell, resulting in a loss of open-circuit voltage (OCV) and a corresponding loss of cell efficiency. One of the purposes of this work is to demonstrate that, provided the cell temperature is maintained at 600 °C or less, the internal current leak within the cell is near-negligible under typical operating current densities, and manageable at open-circuit. Consequently, with the cell at a typical operating current density and a potential of 0.6–0.7 V (typical for fuel cell operation), the cell efficiency is virtually identical to a YSZ-based SOFC with the same intrinsic area specific resistance (ASR).

There are distinct advantages in the metal-supported CGO electrolyte approach. Firstly, the low stack operating temperature of 500–600 °C allows the use of low-cost ferritic stainless steel components in both the stack and the balance of plant (BOP) of the system. Secondly, the use of metal substrates facilitates the use of conventional metal joining techniques such as welding to seal the cells into stacks, eliminating problematic ceramic-to-metal seals, which are a major source of unreliability in conventional SOFC stacks.

In this work, an electrochemical model for a Ceres cell is presented, including equations taking into account the mixed-conductivity of the CGO electrolyte and resulting short-circuit current. This model has a number of adjustable parameters, which have been fitted to experimental current–voltage (V–I) curves for a current Ceres production-standard cell. A good fit between model predictions and experimental data has been demonstrated over a range of operating temperatures and fuel compositions. This electrochemical model is then built into a version of a one-dimensional stack model developed by Aguiar et al. [3], and stack performance is modelled under typical operating conditions.

Finally, a proposed design for a 5 kW$_e$ natural-gas fuelled CHP system is presented and simulated, based around the stack model and complete external reforming. An overall electrical efficiency in the range 33–35% is predicted at both full and half power.

2. Electrochemical model of a metal-supported CGO electrolyte fuel cell

2.1. Description of a Ceres fuel cell

A schematic representation of a Ceres metal-supported SOFC is presented in Fig. 1. The steel substrate is typically a 200–300 μm thick foil, and is made porous in the central region by laser-drilling an array of small holes of 10–30 μm diameter. The outer perimeter of the foil is not drilled, and is used to seal the cell into a stack either by welding, brazing or by means of a compressive gasket.

The anode layer is deposited onto the upper-surface of the substrate. The anode is typically a porous nickel–CGO composite cermet, around 15 μm thick. The electrolyte layer is deposited over the anode as a dense 10–15 μm film of CGO. The electrolyte overlaps the anode to seal the edges of the anode. Finally, the cathode layer is deposited over the top of the electrolyte. The cathode consists of a thin electrochemically active lanthanum strontium cobalt ferrite (LSCF)/CGO composite layer and a thicker layer of an LSCF as a current collector. Further details of the materials used can be found in [1,4].

2.2. Description of the mathematical model of the cell

2.2.1. Open-circuit voltage (OCV)

The theoretical open-circuit voltage of a hydrogen fuel cell is calculated using the Nernst equation, which relates the observed cell potential to the Gibb's free energy of the hydrogen oxidation reaction and the partial pressures of the reactants at the electrolyte/electrode interfaces.

$$V_0 = -\frac{\Delta G_{H_2}^\circ}{2F} - \frac{R_m T}{2F} \ln\left(\frac{p_{H_2O}^{inter}}{p_{H_2}^{inter}(p_{O_2}^{inter})^{0.5}}\right).$$ (1)

However, for a CGO based SOFC, the observed OCV at temperatures in excess of ∼450 °C is depressed by the electronic conductivity of the electrolyte and resulting internal short-circuit.

2.2.2. Current density

For any electrochemical cell, the rate of the electrode reaction is directly proportional to the current density applied through the following well-known relationship:

$$r = \pm\frac{j}{nF}.$$ (2)

However, for a fuel cell with a mixed-conducting electrolyte, the current density representing the flux of oxygen through the electrolyte (j_I) is equal to the sum of the current density applied through the external circuit (j_T) and the current density as a result of internal short-circuiting through the electrolyte (j_E). Thus,

$$j_I = j_T + j_E.$$ (3)

2.2.3. Cathode potential

The cathode potential based upon the oxygen partial pressure on the air side is calculated as [5]:

$$V_{0C} = -\frac{R_m T}{4F} \ln(p_{O_2}^{inter}).$$ (4)

2.2.4. Activation overpotentials of the electrodes

The activation overpotentials of the electrodes represent the amount of energy expended in driving the electrode reactions at a certain rate, and in effect are a measure of the catalytic activity of the electrodes, since the more catalytically active an electrode is for a particular reaction (oxygen reduction in the case of the cathode, hydrogen oxidation in the case of the anode), the lower the activation overpotential for a given current density. A model is required for the activation overpotential of both electrodes as a function of temperature and reactant partial pressure. A non-linear Butler–Volmer type relationship is often used to relate activation overpotentials to current density, which in this case is the current density j_I defined in Section 2.2.2.
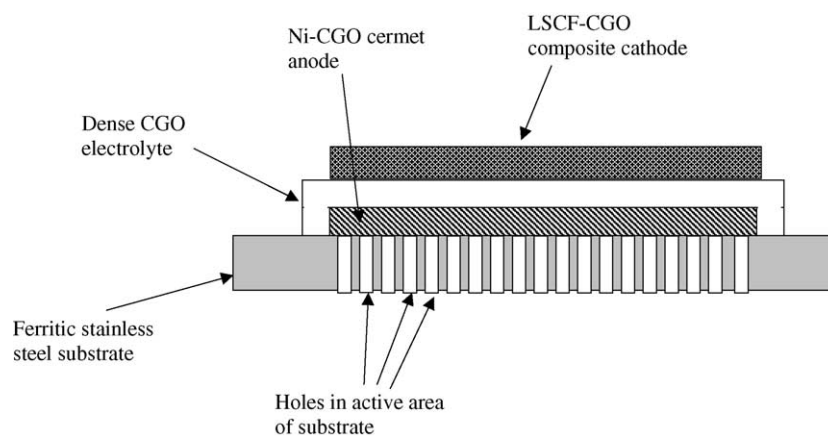

Fig. 1. Schematic diagram of a Ceres Power metal-supported IT-SOFC cell.

For the cathode, this is expressed as:

$$j_I = j_C^0 \left[\exp\left(\frac{F\delta V_C^{act}}{R_m T} \right) - \exp\left(\frac{-F\delta V_C^{act}}{R_m T} \right) \right], \qquad (5)$$

and for the anode as:

$$j_I = j_A^0 \left[\exp\left(\frac{F\delta V_A^{act}}{R_m T} \right) - \exp\left(\frac{-F\delta V_A^{act}}{R_m T} \right) \right], \qquad (6)$$

where j_A^0 and j_C^0 represent the exchange current densities of the anode and cathode, respectively. A typical expression giving the cathode exchange current density as a function of temperature is given in equation (7).

$$j_C^0 = K_C \frac{R_m T}{2F} \exp\left(\frac{-E_{AC}}{R_m T} \right). \qquad (7)$$

A related expression for the anode exchange current density is given in equation (8). In this case, the exchange current density is a function of both temperature and the partial pressure of hydrogen at the anode–electrolyte interface.

$$j_A^0 = (p_{H_2}^{inter})^{0.5} K_A \frac{R_m T}{2F} \exp\left(\frac{-E_{AA}}{R_m T} \right). \qquad (8)$$

The variation of exchange current density with interfacial hydrogen partial pressure to the power of 0.5 was chosen as it gives the best fit to experimental data.

2.2.5. Interfacial reactant partial pressures

With a fuel cell under load, hydrogen and oxygen are consumed in the electrochemical reaction at the interfaces between the electrodes and the electrolyte. On the anode side steam is produced. The reactants are transported to and the products from the electrolyte interfaces by diffusion through the porous electrodes. In order to drive the diffusion process, there has to be a concentration gradient between the interface and the bulk gas stream, and thus the interfacial concentration of the reactants is always lower and that of the products higher than in the bulk gas phase.

In practice, the cathode in a Ceres cell is thin and very porous, and thus the concentration gradient across it is negligible under all normal operating current densities. In addition, air is normally fed to the cell or stack in large excess, and thus the oxygen partial pressure does not change significantly within a stack, meaning that the exchange current density expression in equation (7) can be considered as independent of oxygen partial pressure.

However, the anode kinetics are sensitive to the interfacial hydrogen partial pressure, and the anode and substrate can represent a barrier to both hydrogen reaching the anode/electrolyte interface and steam diffusing away. A schematic of the diffusion path on the anode side around a single laser drilled hole is illustrated in Fig. 2. Hydrogen diffuses through the hole in the substrate, and then laterally through the anode to reach the reacting surface. This two-dimensional diffusion process means that the interfacial hydrogen partial pressure is spatially distributed within the cell. In order to approximately model this, an average diffusion path is assumed consisting of the sum of the substrate thickness ($\tau_{substrate}$) and half the distance between holes in the substrate ($\tau_{holepitch}$). An average effective diffusivity for the gases in the anode ($D_{eff,anode}$) is also assumed. In a Ceres cell, the distance between holes in the substrate is specified such that the cell performance is not affected by significant mass-transport limitation under normal operating conditions. The interfacial hydrogen and steam concentrations are then predicted by the following equations, assuming one-dimensional steady-state counter diffusion of hydrogen and steam [6–8]:

$$p_{H_2}^{inter} = p_{H_2}^0 - \frac{R_m T(\tau_{holepitch} + \tau_{substrate})}{2F D_{eff,anode}} j_I, \qquad (9)$$

$$p_{H_2O}^{inter} = p_{H_2O}^0 + \frac{R_m T(\tau_{holepitch} + \tau_{substrate})}{2F D_{eff,anode}} j_I. \qquad (10)$$

Likewise, assuming one-dimensional self-diffusion of oxygen in nitrogen through the cathode, the interfacial oxygen partial pressure can be estimated by equation (11), although, as mentioned before, the difference from the bulk value is
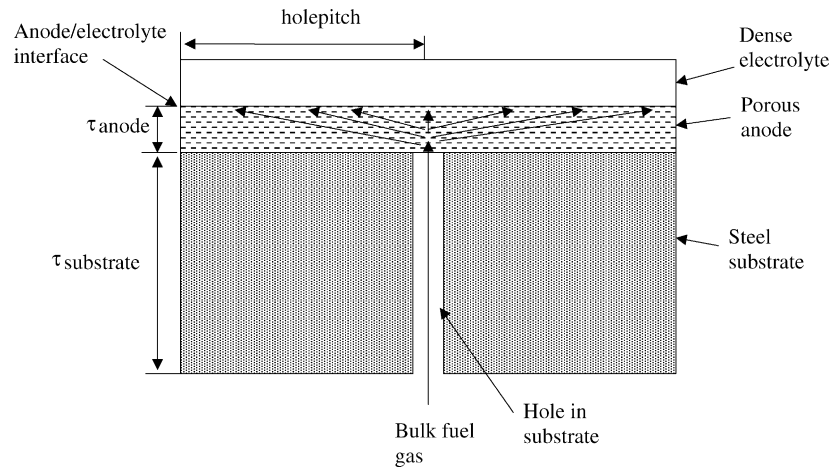

Fig. 2. Schematic of the hydrogen diffusion path through the substrate and anode of a Ceres metal-supported IT-SOFC cell (not to scale).

generally negligible.

$$p_{O_2}^{inter} = P - (P - p_{O_2}^0) \exp\left(\frac{R_m T \tau_{cathode}}{4FD_{eff,cathode}P} j_I\right). \quad (11)$$

2.2.6. Ohmic resistance of the cell

The ohmic resistance of the cell is the sum of the resistance to electronic current flow of the anode and cathode materials (the metallic substrate is assumed to have negligible resistance), and the resistance to ionic current flow of the electrolyte. There is also a contact resistance term R_{cont}, which takes into account the contact resistance between the cathode current collector (a metal mesh) and the cathode.

$$R_{ohm} = \frac{\tau_{anode}}{\sigma_{anode}} + \frac{\tau_{cathode}}{\sigma_{cathode}} + \frac{\tau_{el}}{\sigma_{eli}} + R_{cont}. \quad (12)$$

The values of the anode and cathode current collection resistance were taken as constant with temperature. The ionic conductivity of the CGO electrolyte can be estimated as [5]:

$$\sigma_{eli} = K_i \frac{\exp(-0.64/(8.6173 \times 10^{-5} T))}{T}. \quad (13)$$

2.2.7. Electronic conductivity of the CGO electrolyte and calculation of the electronic leakage current density

The electronic conductivity of the CGO electrolyte can be estimated as [5]:

$$\sigma_{ele} = 3.459 \times 10^{11} \frac{\exp(-2.475/(8.6173 \times 10^{-5} T)) p_{O_2 local}^{-0.25}}{T}. \quad (14)$$

Note that the ionic conductivity of CGO is purely a function of temperature, but that the electronic conductivity is a function of both temperature and the local oxygen partial pressure ($p_{O_2 local}$). The electronic conductivity of CGO is negligible at temperatures below 450 °C and/or in an oxidising environment. However, the oxygen partial pressure in a reducing fuel environment at the temperatures of interest is typically in the range 10^{-20}–10^{-30} bar, and under these conditions CGO can exhibit significant electronic conductivity, depending upon the operating temperature.

An important parameter in calculating the magnitude of the mixed conductivity of CGO electrolytes is p^θ, the value of the oxygen partial pressure at which the ionic and electronic conductivities of the CGO electrolyte are equal. Thus,

$$p_{O_2 local} = p^\theta, \quad (15)$$

when

$$\sigma_{eli} = \sigma_{ele}. \quad (16)$$

Substituting equations (15) and (16) into equations (13) and (14) enables the value of p^θ to be calculated.

The calculation of the electronic leakage current through the electrolyte is rather complex, as it depends on a number of factors:

- the operating temperature;
- the oxygen partial pressure gradient across the electrolyte;
- the thickness of the electrolyte;
- the ionic conductivity of the CGO (which can be significantly reduced by the presence of impurities at the grain boundaries [9]);
- the electrode polarisation resistance;
- the current density.

The effect of the latter is particularly pertinent, because as the current density is increased the average oxygen partial pressure in the electrolyte also increases. This has the effect of reducing the electronic conductivity of the electrolyte and thus the electronic leakage current density. Thus, provided the operating current density of the fuel cell is sufficiently high, the electronic leakage current is negligible, and the efficiency of the cell is not impaired.

The electronic leakage current density is calculated using equation (17).

$$j_E = \left(\frac{p^\theta}{\exp\left(\frac{-4R_m T}{F(V_{0C} + \delta V_C^{act})}\right)}\right)^{1/4} j_I \times \frac{\exp\left[\frac{F}{R_m T} V_{cell} - 1\right]}{1 - \exp\left[-\frac{F}{R_m T} j_I \frac{\tau_{el}}{\sigma_{eli}}\right]}. \quad (17)$$

The derivation of this equation is discussed in [5], but is based upon an expression originally derived by Riess [10].

2.2.8. Calculation of cell terminal voltage

The cell terminal voltage can be calculated as:

$$V_{cell} = V_0 - (j_I R_{ohm} + \delta V_A^{act} + \delta V_C^{act}). \quad (18)$$

If the temperature, bulk hydrogen and steam partial pressures and the operating current density j_T are specified, the cell terminal voltage can be calculated by the simultaneous solution of equations (1), (3)–(18). Note that as a number of the equations are implicit and non-linear, the only practical solution method is numerical iteration.

2.3. Solution procedure and parameter fitting to experimental data

2.3.1. Numerical simulation procedure

The simultaneous equations described in Section 2.2 were encoded for computer simulation using the gPROMS Version 2.3.1 equation-based dynamic process simulation package [11]. To simulate the polarisation curve of a fuel cell, the external current density j_T was made equal to the elapsed time of the simulation, with a small offset at zero time/current to avoid divide-by-zero errors in the mathematical model. Thus, a plot of cell terminal voltage versus time is directly equivalent to a plot of cell terminal voltage versus applied current density, which is available experimentally.

gPROMS has a sophisticated parameter-fitting functionality which enables a set of parameters to be derived for a particular mathematical model which give the best model fit to multiple sets of experimental data taken under different initial conditions. This technique was used to extract the optimum model parameters to fit a set of *V–I* curves for a particular class of fuel cell taken under a range of temperatures and fuel compositions.

2.3.2. Experimental procedure

The experimental data used for parameter fitting were taken from a current Ceres production-standard cell. These cells have been reproducibly manufactured at the hundreds-off scale and are well characterised. However, they do not by any means represent the final performance achievable, as there remains much scope for optimisation of all cell components. Indeed, recent results in our cell development programme have demonstrated power densities of $0.5\,W\,cm^{-2}$ at $600\,^{\circ}C$ when operating on moist hydrogen/air.

A standard cell (active area of $15.2\,cm^2$) was tested using a standard Ceres metallic test housing. Both fuel and air were supplied at a rate of $450\,s\,cm^3\,min^{-1}$ such that depletion of hydrogen and oxygen would be minimal across the cell. The hydrogen supply was humidified by bubbling it through deionised water. For the tests at lower hydrogen partial pressures, the hydrogen was diluted with argon, but the total flow-rate of gas over the anode side of the cell remained constant.

After the cell had been heated to $600\,^{\circ}C$ and left for a few hours to stabilise, *V–I* curves were measured at cell temperatures of $600\,^{\circ}C$, $570\,^{\circ}C$ and $550\,^{\circ}C$. At each temperature three different fuel compositions were used, giving various hydrogen partial pressures. The three gas mixtures used were 97% H_2 and 3% H_2O, 68.5% H_2, 28.5% Ar and 3% H_2O, and 48.5% H_2, 48.5% Ar and 3% H_2O. It has been shown in stack testing, where the test system allows high mole fractions of steam to be injected into the fuel stream, that the performance

Table 1
Fixed parameters in metal-supported IT-SOFC electrochemical model for a metal-supported IT-SOFC cell

Parameter	Description	Value
τ_{anode} (m)	Anode thickness	1.5×10^{-5}
$\tau_{substrate}$ (m)	Substrate thickness	3.0×10^{-4}
$\tau_{holepitch}$ (m)	Substrate hole spacing	1.25×10^{-4}
$\tau_{cathode}$ (m)	Cathode thickness	5.0×10^{-5}
τ_{el} (m)	Electrolyte thickness	1.5×10^{-5}
σ_{anode} ($S\,m^{-1}$)	Anode electrical conductivity	8.0×10^4
$\sigma_{cathode}$ ($S\,m^{-1}$)	Cathode electrical conductivity	8.4×10^3
K_C ($S\,m^{-2}$)	Cathode pre-exponential factor	7.0×10^{11}
K_A ($S\,m^{-1}\,bar^{-0.5}$)	Anode pre-exponential factor	3.2×10^{13}

Table 2
Extracted parameters in metal-supported IT-SOFC electrochemical model giving the best fit to experimental data for a metal-supported IT-SOFC cell

Parameter	Description	Value
R_{cont} ($\Omega\,m^2$)	Contact resistance	8.46×10^{-6}
$D_{eff,anode}$ ($m^2\,s^{-1}$)	Anode effective diffusivity	1.495×10^{-6}
E_{AC} ($J\,mol^{-1}$)	Cathode activation energy	1.309×10^5
E_{AA} ($J\,mol^{-1}$)	Anode activation energy	1.294×10^5
K_i ($S\,K\,m^{-1}$)	Ionic conductivity pre-exponential factor	2.706×10^6

of the fuel cell is dependent upon the dilution of the hydrogen rather than what it is diluted with.

2.3.3. Parameters used in the computer model

A number of parameters in the model, particularly those relating to the physical dimensions of the fuel cell, were fixed. These parameters and their values are listed in Table 1. A second set of parameters were used for the parameter estimation process. These are listed in Table 2 along with the values giving the optimum fit to the experimental data. Specifically the contact resistance term, R_{cont}, includes the contact resistance and any other temperature invariant ohmic resistances in the cell. The anode effective diffusivity ($D_{eff,anode}$) takes into account the effective porosity of both the anode and the substrate, and thus the resistance to hydrogen/steam transport to/from the anode/electrolyte interface.
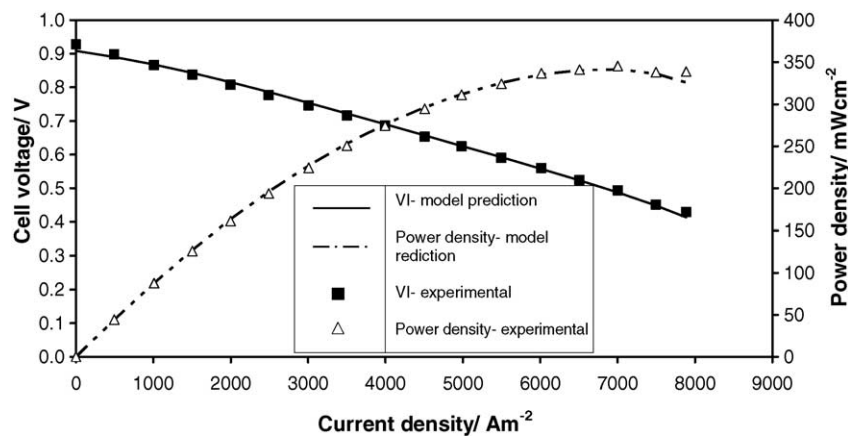

Fig. 3. Comparison of model-predicted and experimental *V–I* and power curves for a metal-supported IT-SOFC cell at $600\,^{\circ}C$ and 97% H_2/3% H_2O.
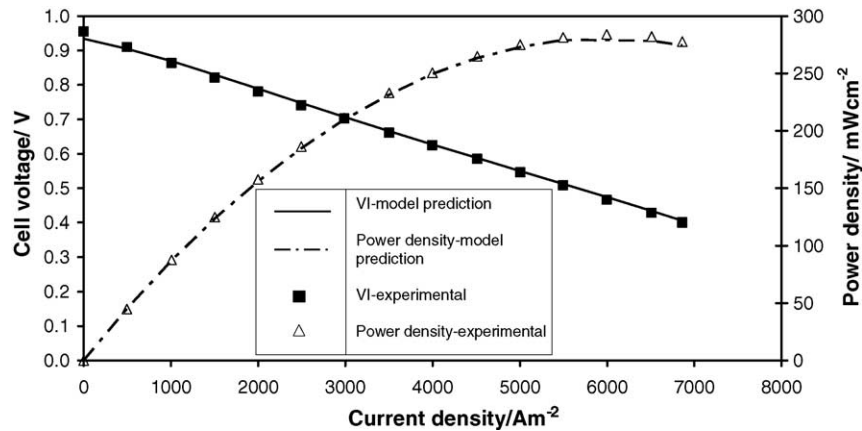
Fig. 4. Comparison of model-predicted and experimental V–I and power curves for a metal-supported IT-SOFC cell at 570 °C and 97% H_2/3% H_2O.

The anode and cathode activation energy terms relate to the temperature variation of the anode and cathode exchange current densities as calculated in equations (7) and (8). The ionic conductivity pre-exponential factor (K_i) relates to the ionic conductivity of the CGO electrolyte, together with other thermally activated ohmic resistances in the cell.

2.3.4. Results and discussion

A comparison between experimental and model-predicted V–I and power curves are presented in Figs. 3–9. A comparison of results was made over the temperature range 550–600 °C, and between 48.5% and 97% hydrogen. The first point to note is that the fuel cells produce a maxi-
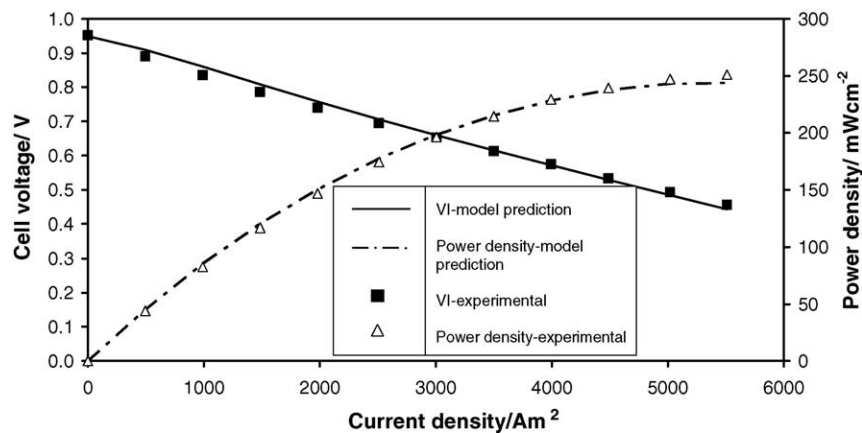

Fig. 5. Comparison of model-predicted and experimental V–I and power curves for a metal-supported IT-SOFC cell at 550 °C and 97% H_2/3% H_2O.
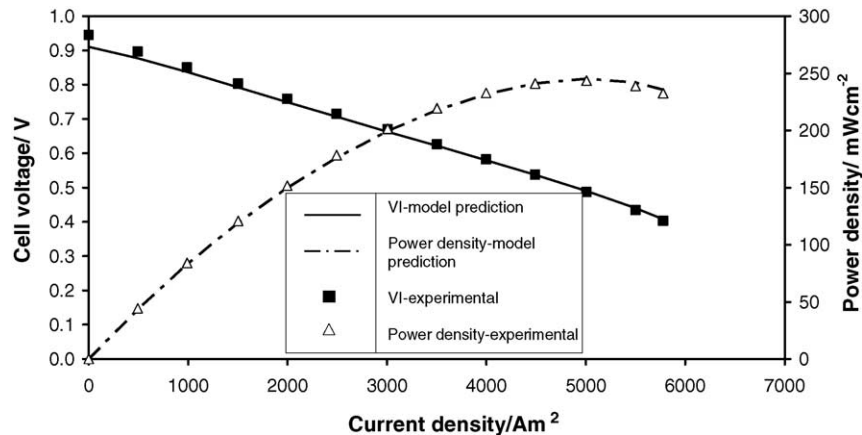

Fig. 6. Comparison of model-predicted and experimental V–I and power curves for a metal-supported IT-SOFC cell at 570 °C and 68.5% H_2/28.5% Ar and 3% H_2O.
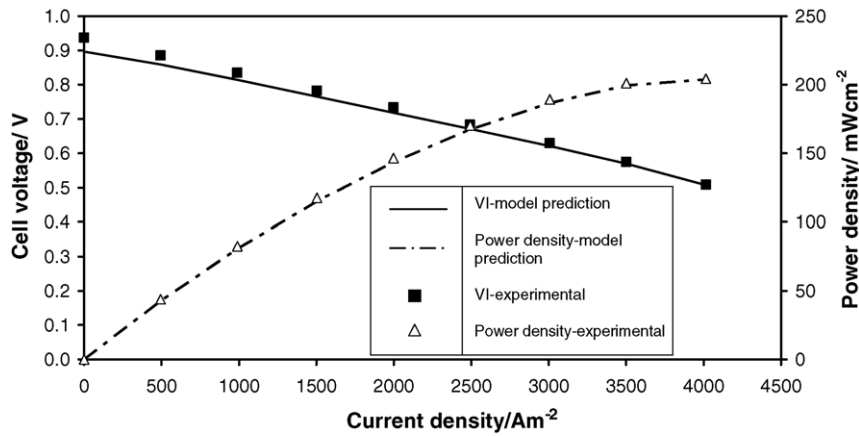
Fig. 7. Comparison of model-predicted and experimental V–I and power curves for a metal-supported IT-SOFC cell at 570 °C and 48.5% H_2/48.5% Ar and 3% H_2O.
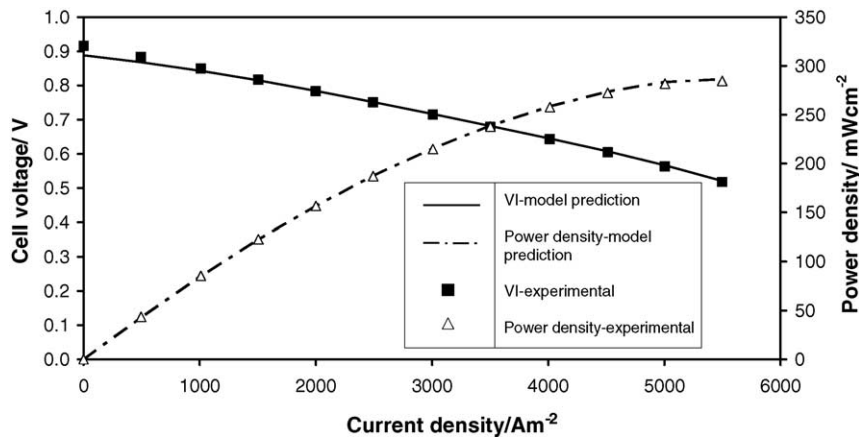

Fig. 8. Comparison of model-predicted and experimental V–I and power curves for a metal-supported IT-SOFC cell at 600 °C and 68.5% H_2/28.5% Ar and 3% H_2O.

mum power density around 250–350 mW cm^{-2} at a temperature between 550 °C and 600 °C when operated on 97% hydrogen/air. Also of note is the good quality of the fit between the experimental data and the model under all the test conditions.

The open-circuit voltage of the cell is somewhat depressed by comparison with the theoretical open-circuit potential of a hydrogen fuel cell of 1.05–1.10 V. This is as a result of the electronic leakage through the CGO electrolyte at open-circuit. Fig. 10 shows the model-predicted electronic leak-

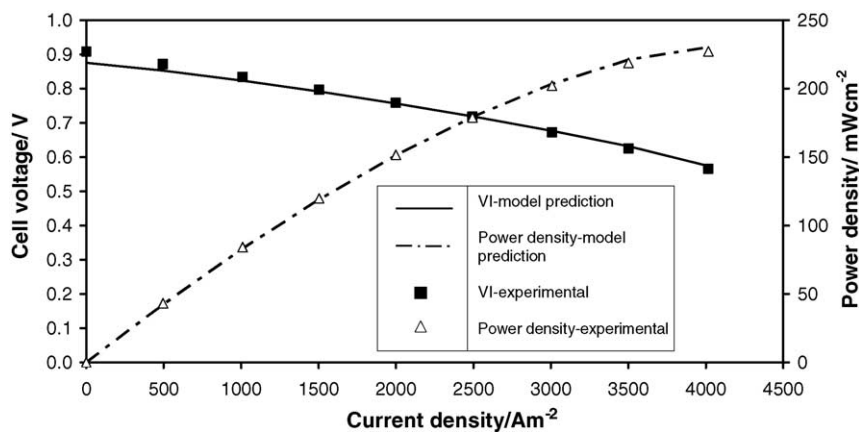Fig. 9. Comparison of model-predicted and experimental V–I and power curves for a metal-supported IT-SOFC cell at 600 °C and 48.5% H_2/48.5% Ar and 3% H_2O.
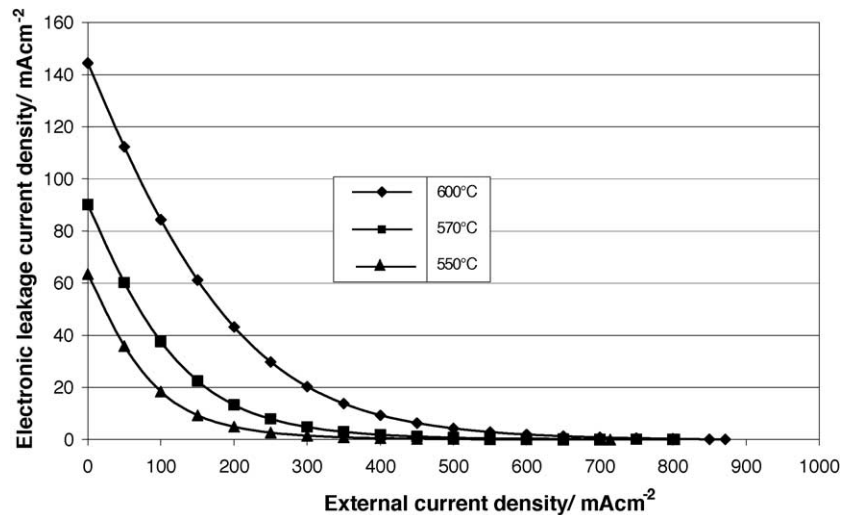
Fig. 10. Model-predicted electronic leakage current density through the CGO electrolyte as a function of external circuit current density and temperature with a fuel mixture of 97% H_2/3% H_2O.

age current density as a function of temperature and external circuit current density. As expected, the electronic leakage current density increases with increased temperature, but falls sharply with applied external current density. Indeed, at a typical operating current density of $300\,mA\,cm^{-2}$ and at $600\,°C$, the predicted electronic leakage current density is only $20\,mA\,cm^{-2}$ or 6.3% of the total current, demonstrating that the loss of cell efficiency as a result of the mixed conductivity of the electrolyte is negligible. At lower temperatures, the electronic leakage current is even lower.

3. Stack model based around metal-supported CGO SOFCs

3.1. Introduction

The electrochemical model described in the previous section was developed to accurately simulate the performance of a Ceres IT-SOFC cell over a range of temperatures and fuel partial pressures. This model was then built into a dynamic model of a planar SOFC stack, building on that developed by Aguiar et al. [3] to model an internal reforming planar IT-SOFC stack based upon anode supported cells with YSZ electrolytes. This model was used in the form described in [3], other than the inclusion of the CGO electrochemical model described previously. The reactant utilisation and heat generation from the electronic leakage in the electrolyte were included in the mass and heat balances of the stack model, respectively. The potential loss of efficiency resulting from the use of CGO electrolytes has therefore been accurately simulated.

To produce a useful voltage, a SOFC consists of several repeating electrochemical cells in a module, connected both in series and/or in parallel and assembled to compose a stack. However, SOFC models are usually developed for the small-

est unit cell or module, then used to compute the operating conditions of the whole stack. In the case reported here, the repeating single-cell is considered to be in the centre of a large stack, such that no edge effects are present, and to be formed when two interconnect plates are placed above and below the cell PEN structure. A schematic side view of a co-flow SOFC stack, where the unit cell being modelled is indicated, is illustrated in Fig. 11. For the model, the SOFC was considered to be composed of fuel and air channels, PEN structure, and interconnect. The model consists of mass balances around the fuel and air channels, energy balances around the fuel and air channels, PEN, and interconnect, and the electrochemical model that relates the fuel and air gas compositions and the various cell temperatures to voltage, current density, and other cell variables. The chemical species considered are CH_4, H_2O, CO, H_2, and CO_2 for the fuel stream and O_2 and
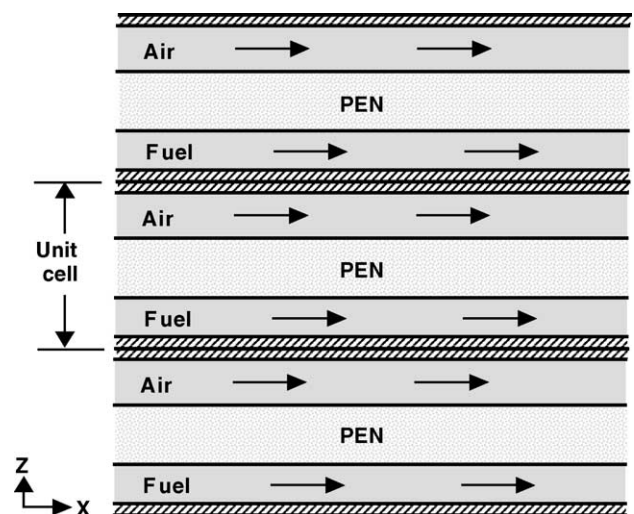

Fig. 11. Schematic side view of a co-flow planar SOFC stack showing the unit cell.

N_2 for the air stream. It is assumed that only H_2 is electro-chemically oxidised, with all the CO converted through the water–gas shift reaction, assumed at equilibrium, and any CH_4 in the fuel can only be reformed to H_2, CO, and CO_2 but not electrochemically oxidised. The model retains the ability to internally reform methane, but for all the simulations presented complete or near-complete external reforming is assumed.

For the model solution, in addition to all geometry and property data and inlet temperatures and compositions, it is necessary to specify the average current density, fuel utilisation, and air ratio (from which the molar flux of fuel and air are determined). Fuel utilisation is defined as the fraction of the inlet fuel that is used to produce electricity, and the air ratio as the excess air, in relation to that stoichiometrically needed, that is supplied for cooling.

The complete model consists of a system of simultaneous partial differential and algebraic equations, which is solved using gPROMS ModelBuilder 2.3.1 [11], with the finite difference integration method. All remaining details of the model developed can be found in [3] and Section 2 of this paper.

3.2. Details of the simulation

The results presented in this paper are based around a 2.5 kW$_e$ stack operating on a completely externally reformed hydrocarbon fuel with co-flow of the fuel and air streams.

Table 3
Fixed parameters in metal-supported IT-SOFC stack model

Parameter	Value
Number of array plates in stack	140
Fuel utilisation (%)	70
Stoichiometric air ratio	12.2
dc power output (W)	2500
Fuel channel hydraulic mean diameter (mm)	0.5
Fuel channel hydraulic mean diameter (mm)	1.0
Fuel inlet temperature (°C)	500
Air inlet temperature (°C)	500

Table 4
Composition of fuel gas fed to metal-supported IT-SOFC stack model

Fuel component	Mole percentage
Methane	0.6
Carbon monoxide	9.4
Hydrogen	51.5
Carbon dioxide	9.0
Steam	29.5

The stack geometry was based upon an active cell area per bipolar array plate of 121 cm^2 as a square array of nine square cells each with an active surface area of 37 mm × 37 mm. A schematic bipolar array plate is illustrated in Fig. 12. The major stack operating parameters are listed in Table 3, and the assumed fuel composition (based upon the near-complete external reforming of propane at a steam/carbon ratio of 3.0) is listed in Table 4.
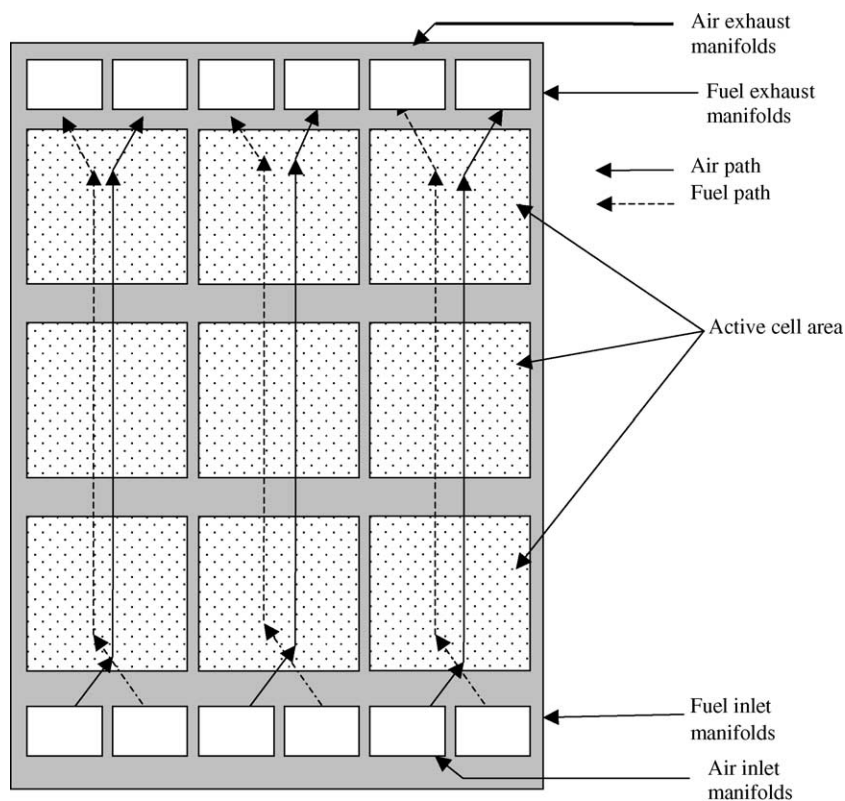

Fig. 12. Schematic of a 9-cell co-flow array bipolar plate, showing internal manifolds.

Table 5
Predicted performance of metal-supported IT-SOFC stack

Variable	Value
Stack external current (A)	26.7
Stack voltage (V)	93.7
Mean cell voltage (V)	0.670
Stack mean external current density (mA cm^{-2})	221
Stack mean power density (mW cm^{-2})	148
Stack LHV efficiency (%)	35.2
Air outlet temperature (°C)	629
Fuel outlet temperature (°C)	630
Maximum cell temperature gradient (K mm^{-1})	1.46
Mean electronic leakage current (A)	1.1
Mean electronic leakage current density (mA cm^{-2})	9.1
Fuel flow rate (kg s^{-1})	5.9×10^{-4}
Air flow rate (kg s^{-1})	1.69×10^{-2}

3.3. Results and discussion

The predicted stack performance is illustrated in Table 5. Note that the lower heating value (LHV) efficiency is based upon the energy content of the reformate fuel, not the original hydrocarbon. If the energy for reforming the hydrocarbon fuel is supplied from waste heat from the stack, the equivalent stack efficiency based upon the original hydrocarbon fuel would be in excess of 40%. Fig. 13 shows the predicted temperature profiles along the length of the fuel channel in the direction of gas flow for the air, fuel and cell structure. Fig. 14 shows the predicted distribution of current density along the same axis. The external current density, electronic leakage current density and the total ionic current density in the electrolyte are shown.

Finally, Fig. 15 shows the predicted distribution of fuel gas composition in the direction of fuel flow across the cells. A small amount of methane was fed in the fuel, reflecting some assumed hydrocarbon slippage from the external reformer. It can be seen from Fig. 15 that the level of methane in the fuel mixture is predicted to rise slightly initially, as a result of the methanation reaction:

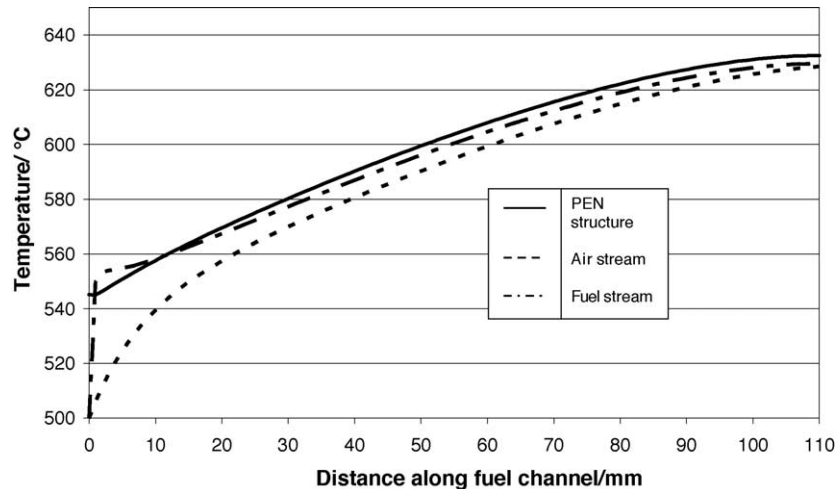$$CO + 3H_2 \rightarrow CH_4 + H_2O \tag{19}$$

Fig. 13. Predicted temperature profiles of the air stream, fuel stream and PEN structure of a co-flow planar IT-SOFC stack along the direction of fuel flow.
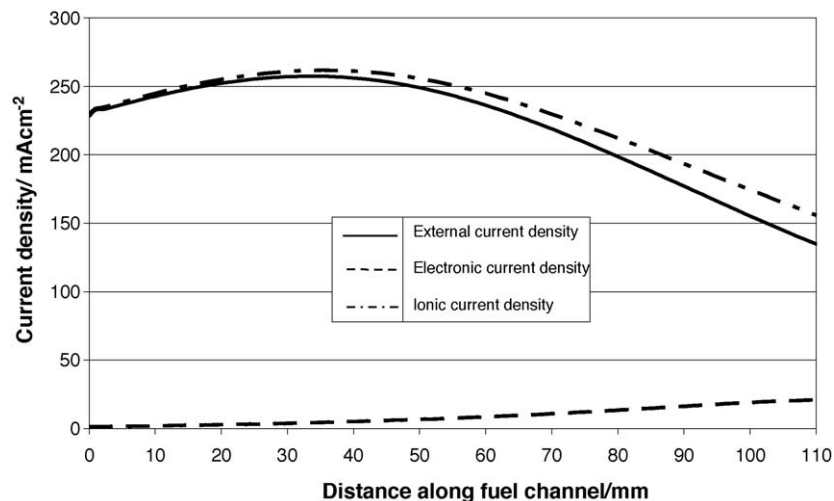

Fig. 14. Predicted external, ionic and electronic leakage current densities of a co-flow planar IT-SOFC stack along the direction of fuel flow.
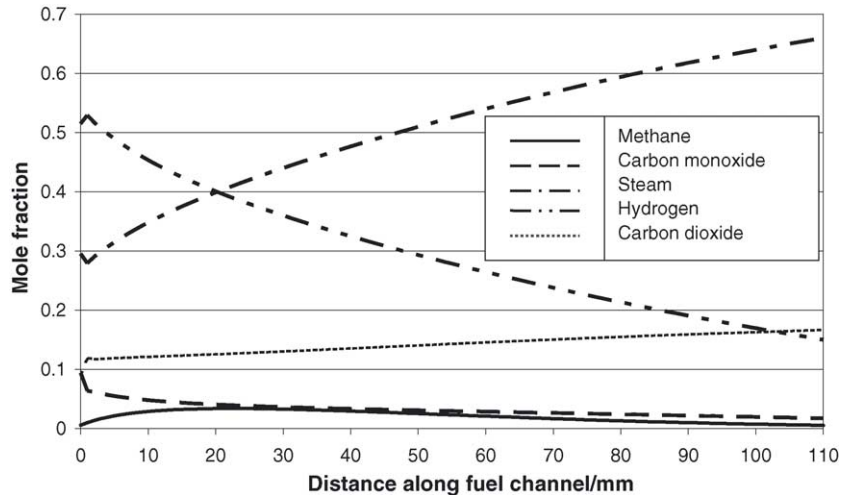
Fig. 15. Predicted fuel stream composition changes of a co-flow planar IT-SOFC stack along the direction of fuel flow.

The concentration of methane in the fuel stream is then predicted to fall again to very low levels further along the fuel channel as the temperature rises and the concentration of CO and hydrogen falls, forcing the equilibrium of reaction (19) back to the left. The rapid change in reactant concentrations near the inlet to the stack is as a result of the reequilibration of the water gas shift (WGS) reaction (20) from the reformer exit temperature to the lower stack temperature.

$$CO + H_2O \leftrightarrow CO_2 + H_2 \qquad (20)$$
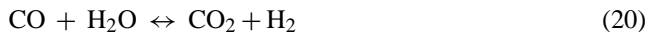
Apart from this, as would be expected, the concentrations of hydrogen and CO fall along the length of the fuel channel, and the concentrations of steam and CO_2 rise. Hydrogen is consumed in the cell reaction, producing steam. CO is consumed by being shifted to hydrogen via the WGS reaction (20), where the equilibrium shifts to the right as partial pressure of hydrogen falls and that of steam rises.

The distribution of current density seen in Fig. 14 is as a result of the variation in temperature and hydrogen partial pressure along the direction of flow. The cells are assumed to be at a constant potential because of the high conductivity of the anode and substrate. The variations in cell area specific resistance (ASR) as a function of temperature and hydrogen partial pressure therefore manifest themselves as a spatial variation in current density. The predicted external current density initially rises along the direction of fuel flow, as a result of increasing temperature, before falling off again as the depletion of the hydrogen in the fuel towards the exit becomes dominant over the temperature.

As would be expected, the electronic leakage current density increases along the direction of fuel flow with increasing temperature. However, even at 630 °C the electronic leakage current density is only of the order of 21 mA cm^{-2}. This is partly because the electronic leak is a function of both temperature and oxygen partial pressure on the fuel side. As the hydrogen becomes depleted, and the H_2/H_2O ratio falls, the oxygen partial pressure in the fuel stream rises, resulting in a less reducing atmosphere and hence less reduction of the CGO.

The temperature profile in Fig. 13 is as a result of the heat generation within the cells resulting from current flow through the internal resistance of the cells. This heat is dissipated by transfer to the gas streams, particularly the air stream. A temperature rise of 130 K across the stack is predicted for the air stream. Because the fuel flow is much lower than the air flow, the fuel stream very rapidly heats to the temperature of the metal components at the entry to the fuel channel. A larger temperature difference exists between the air and the metallic components because of the higher heat capacity of the air stream, and also the lower heat transfer coefficient between the air and the metallic components by comparison with a gas containing a high fraction of hydrogen. It is anticipated that the temperature profile would be flatter if the model included heat loss through the walls, and this is the subject of on-going work.

4. Modelling of a 5 kW$_e$ natural gas fuelled combined heat and power system with external reforming based upon metal-supported CGO SOFCs

4.1. Introduction

A highly attractive application for SOFCs is small-scale combined heat and power, which gives the option to significantly increase the overall efficiency of power generation by recovering the waste heat, which is usually discharged to the environment in centralised power generation. SOFCs are particularly well suited to systems involving heat recovery, because their high operation temperature means the waste heat is of high grade. The high-grade of waste heat from an SOFC stack also means SOFCs are well suited to efficient operation on reformed hydrocarbon fuels, since the waste heat from the stack can be used to steam-reform hydrocarbons without the need to burn additional primary fuel.

Many system concepts exist, but that presented here is based around two 2.5 kW$_e$ metal-supported IT-SOFC stacks producing a maximum electrical power output of 5.1 kW$_e$ gross, 4 kW$_e$ net after parasitic losses, operating on externally steam-reformed natural gas. The system has heat recovery from the exhaust gas giving a sustained thermal output of 5.2 kW. The system is predicted to have a net electrical efficiency of around 35%, demonstrating that it is possible to build an IT-SOFC system based around cells with CGO electrolytes with an efficiency which is significantly higher than existing technologies of equivalent power rating. The overall efficiency is predicted to be around 80%.

Parallel studies of system concepts incorporating other fuel processing strategies such as partial oxidation reforming and internal reforming are on-going, and will be reported separately.

4.2. Description of the simulated system

4.2.1. Overview

The design philosophy for this system was based upon achieving the highest possible overall efficiency (electrical and thermal) consistent with external reforming of the fuel. External reforming was selected for this analysis as it allows parallel development of both the reforming sub-system and the fuel cell sub-system, reducing technical risk. External reforming also brings the advantage of simplicity, an important characteristic for small stand-alone fuel cell systems. However, the disadvantage of external reforming is that the endothermic reforming reaction no longer provides cooling to the stack, increasing the stoichiometric air ratio (the ratio of the actual air supplied to that required to meet the oxygen demand of the cell reaction), with an associated efficiency penalty because of the high power requirement for the blower which supplies air to the system. In addition the high air mass flow lowers the stack exhaust temperature, impacting on the efficacy of waste heat recovery.

In order to achieve a system design which mitigates against high air flow rate requirements, a design was adopted where the 5 kW$_e$ power output is achieved with two 2.5 kW$_e$ stacks. The fuel supplies for the stacks are connected in parallel. The two stacks are connected in series on the air side, with an intercooler between the stacks. This is a heat exchanger to remove the heat input from the first stack by cooling its cathode exhaust stream with the cold incoming air stream. In this way, the air requirement to provide stack cooling is effectively halved, at the expense of a somewhat higher system air pressure drop. A process flowsheet of the proposed system is presented in Fig. 16, and discussed in the following.

4.2.2. Fuel supply sub-system

Natural gas fuel is supplied through a suitable mass flow controller in the natural gas feed. The natural gas is assumed to be a mixture of 97% methane and 3% propane. The fuel is mixed with steam at a steam/carbon (S/C) ratio of 3.0 in the fuel mixer, and fed to the reformer R1. The reformer is

heated by hot exhaust gas from the stack, with the excess fuel in the anode off-gas burned off in afterburner B1. Hot reformate from the reformer at around 650 °C is fed directly to the stacks with the fuel feed split equally between the two stacks. A conversion of hydrocarbons in excess of 95% is achieved in the reformer. Steam for the reformer is supplied via the evaporator EV1. This takes a supply of cold water from the water tank, which is fed through a metering pump P1 to control the mass flow of water proportional to the mass flow of fuel, in order to achieve the desired steam/carbon ratio. The evaporator is a flash evaporator heated by the exhaust gas from the system.

4.2.3. Air supply sub-system

Air is supplied at ambient temperature and pressure to the air blower C1, which drives the air through the system. The compressor includes a mass flow meter for the air and a variable speed motor control. Air mass flow is therefore controlled by varying the fan motor speed. The stack temperature controller supplies the setpoint for the required air mass flow, and stack temperature is regulated by varying the air flow, and thus the degree of cooling provided. The air from the blower is fed to the intercooler HX1. The intercooler is a heat exchanger which uses the cold incoming air stream to cool the cathode exhaust gas from stack 1 prior to feeding it to stack 2. The intercooler is fitted with a bypass on the cold side, regulated by a valve BPV1. The purpose of this is to regulate the degree of cooling provided such that the temperature of the air entering stack 2 is kept constant. This is important in terms of stabilising the overall stack temperature control loop and also when trying to keep the two stacks at the same temperature.

The partially preheated air stream is then fed to the air preheater HX2, which is heated by hot exhaust gas. The air is preheated to 480 °C prior to being fed to stack 1. Again temperature control is provided by partially bypassing cold air around the heat exchanger via valve BPV2, which enables the air temperature entering stack 1 to be maintained at 480 °C. The preheated air stream is then fed to stack 1. The air is heated from 480 °C to around 615 °C in the stack, and then fed to the other side of the intercooler where it is cooled back to 480 °C prior to being fed to stack 2. The air exhaust from stack 2, again at around 615 °C, is fed to the afterburner along with the fuel exhausts from both stacks.

4.2.4. Exhaust sub-system

The fuel exhausts from both stacks and the air exhaust from stack 2 are fed to the afterburner B1. This is a catalytic burner to consume the fuel not used within the stack. The hot gas from the burner is fed initially to heat the reformer. In practice, the reformer and catalytic afterburner would be integrated as a single unit. The exhaust gas is then fed to the steam generator EV1, and used to heat this to raise steam. After the evaporator, the exhaust gas is fed to the air preheater HX2, where most of its heat is recovered to preheat the air feed to the stack. Any residual heat in the exhaust gas
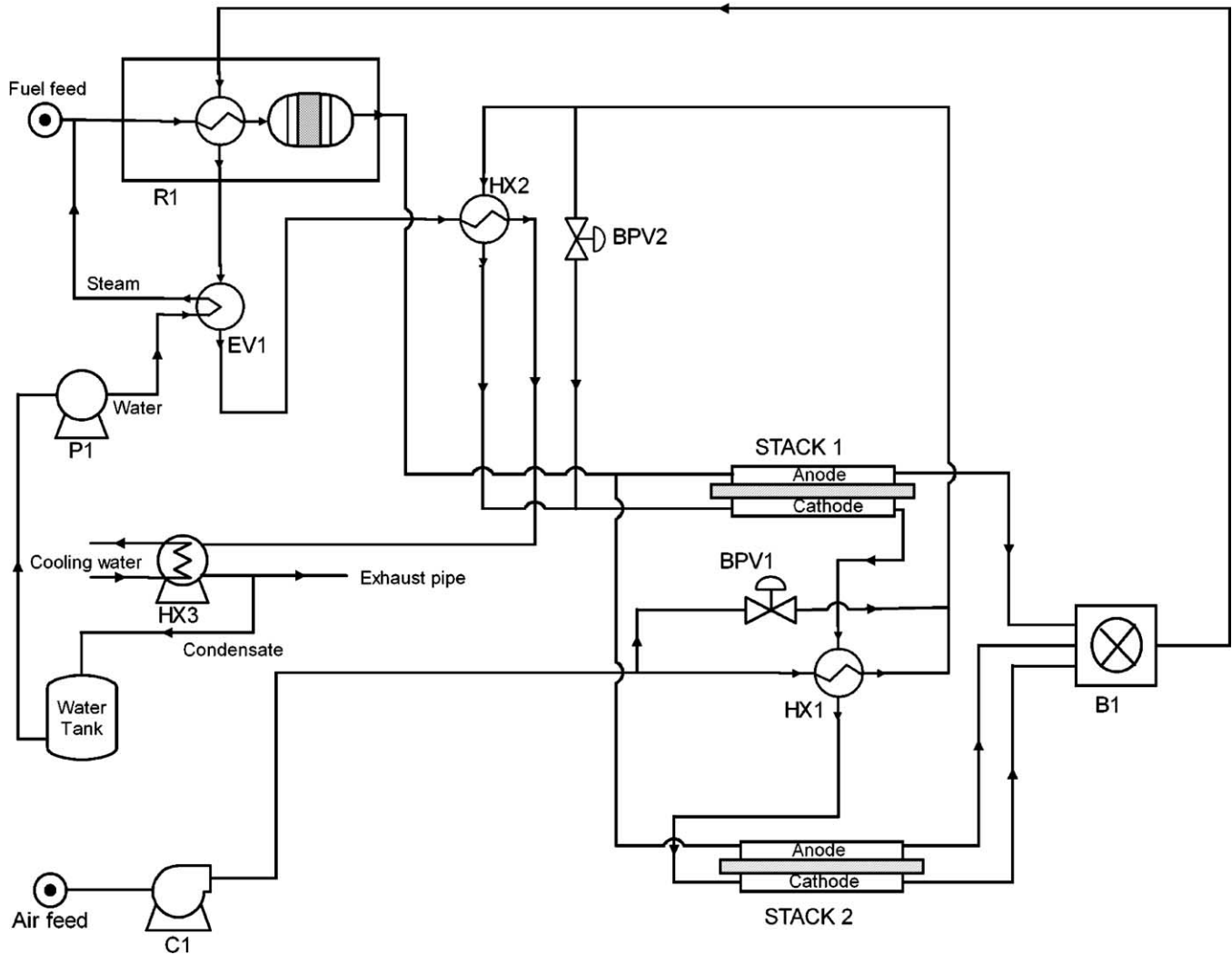
Fig. 16. Process flowsheet of proposed natural-gas-fuelled IT-SOFC CHP system.

is then effectively waste heat, which can be recovered and used for space heating or evaporative cooling as part of the combined heat and power system. The waste heat is recovered in heat exchanger HX3, where it is used to heat water supplied at 50 °C and heated to 90 °C. The exhaust temperature is reduced to 55 °C, which is below the dew-point of the gas mixture since it contains a significant mole fraction of steam. A percentage of the steam is therefore condensed out, releasing its latent heat of evaporation and improving the heat recovery. The condensate is returned to the water tank, thus reducing the demand for fresh water to feed the steam generator.

4.3. Details of the computer simulation

A computer model of the IT-SOFC CHP system described in the preceding section was written using the gPROMS Version 2.3.1 dynamic process simulation package. The stacks were modelled using the custom-written model described in this paper. Most of the other components were modelled us-

ing generic component models from the gPROMS Process Model Library (PML). The model is fully dynamic; however, only steady-state results will be presented here.

Apart from the stack, the only major component requiring a custom model was the heated steam reformer. This was modelled as a set of four heat exchangers to heat the fuel stream using the hot exhaust gas, with an adiabatic reformer between each heat exchanger. The heat exchangers are modelled using a one-dimensional dynamic distributed model, which includes the mass and heat capacity of the metal and therefore has a dynamic lag.

Control of the system is provided by a set of four simulated proportional–integral–derivative (PID) control loops as follows:

1. *Stack temperature control*: PID loop controlling the mass flow of air through the stacks to control the degree of cooling. The input signal is taken as the average of the temperatures at the centre of interconnects plates in the middle of both stacks. The output of this loop is the re-

Table 6
Parameters for proposed natural-gas-fuelled IT-SOFC CHP system

Parameter	Value
Stack fuel utilisation (%)	70
Steam/carbon ratio in reformer	3.0
Power conversion efficiency (%)	97
Power for control system (W)	200

quired mass flow of air. This is taken as the setpoint input to a second PID loop in cascade mode, which takes the mass flow of air from a mass flow sensor as its input, and outputs the required fan motor speed to achieve this mass flow.

2. *Stack 1 air inlet temperature control*: PID loop taking the air inlet temperature to stack 1 as its input signal, and controlling this by varying the position of BPV2 to bypass a variable fraction of the supplied cold air around the air preheater HX2.

3. *Stack 2 air inlet temperature control*: PID loop taking the air inlet temperature to stack 2 as its input, and controlling this by varying the position of BPV1 to bypass a variable fraction of cold air around the stack air intercooler HX1, thus varying the degree of cooling of the air stream between the two stacks.

4. *System power control*: PID loop taking the system net power output as its input, and varying the current applied to the stack to maintain the power output constant.

In addition to these control loops, there are two ratio controllers. One which varies the mass flow rate of fuel entering the system directly proportional to the stack current, to maintain a constant fuel utilisation. The second varies the mass flow of water to the evaporator directly proportional to the mass flow of fuel, so as to maintain a constant steam/carbon ratio in the reformer.

The simulation results presented here are at steady state at full power and half power. In both cases, a dynamic simulation was run and allowed to continue until the stack temperature had stabilised to a rate of change of less than $0.1\,\mathrm{K\,min^{-1}}$, and this was taken as the steady state.

Table 6 shows the principal system operating parameters, including the assumed parasitic losses in power conversion and to run the control system. Apart from this, the other major parasitic loss is the electrical power required to drive the air blower, which is dependent upon the air demand and the pressure drop of the system.

5. Results and discussion

The predicted performance of the IT-SOFC CHP unit at 100 and 50% power is illustrated in Table 7. It can be seen that at 100% power in this simulation around $1.1\,\mathrm{kW_e}$ of stack power is lost in parasitic power consumption within the system, predominantly the power required to drive the air blower. The predicted overall electrical efficiency of the

Table 7
Predicted performance of IT-SOFC CHP system at 100% and 50% rated electrical power output

Variable	Description	Value 100% power	Value 50% power
P_{elDC}	Stack dc power output (W)	5140	2583
P_{elAC}	System ac power output (W)	4000	2000
Q_{th}	System heat output (W)	5232	2941
Q_{fuel}	LHV energy input in fuel (W)	11609	6019
λ	Stoichiometric air ratio	5.2	5.0
η_{elAC}	Overall electrical efficiency (%)	34.5	33.2
η_{elDC}	Stack efficiency (%)	44.3	42.9
η_{th}	Thermal efficiency (%)	45.1	48.9
η_{ov}	Overall efficiency (%)	79.5	82.1
m_{fin}	Fuel feed rate (kg h^{-1})	0.839	0.436
m_{ain}	Air feed rate (kg h^{-1})	49.9	25.1
η_{CO_2}	Specific CO_2 emissions (g kWh$_e^{-1}$)	581	603

system is 33–35% based upon the lower heating value (LHV) of the fuel. One important characteristic demonstrated here is that the predicted efficiency of the system does not vary significantly over the range 50–100% power. This constant-efficiency part-load characteristic is very attractive by comparison with conventional internal combustion engine (ICE) based CHP systems.

It can be seen that the overall energy efficiency of the system is predicted to be around 80% when heat recovery is included, and this slightly improves at part load. The improvement in heat recovery efficiency is largely because the heat exchanger area is fixed. All the heat exchangers in the system are sized on the basis of the gas flows required at full power, and are therefore oversized under part-load conditions. This increase in heat exchanger surface area relative to gas flow increases the efficiency of all the heat exchangers at part load.

Table 8 shows the predicted performance of the two stacks under full-load conditions. It can be seen that the stacks are sized on the basis of operating at a design point of 0.7 V per

Table 8
Predicted performance of both stacks in IT-SOFC CHP system at 100% rated electrical power output

Parameter	Stack 1	Stack 2
Stack external current (A)	27.0	27.0
Stack voltage (V)	94.0	94.4
Mean cell voltage (V)	0.691	0.693
Stack mean external current density (mA cm^{-2})	188	188
Stack mean power density (mW cm^{-2})	130	130
Stack centre temperature (°C)	594	597
Air inlet temperature (°C)	480	480
Fuel inlet temperature (°C)	630	630
Air outlet temperature (°C)	637	642
Fuel outlet temperature (°C)	639	644
Mean electronic leakage current (A)	1.2	1.3
Mean electronic leakage current density (mA cm^{-2})	8.3	9.0
Fuel flow rate (kg s^{-1})	5.05×10^{-4}	5.05×10^{-4}
Air flow rate (kg s^{-1})	1.30×10^{-2}	1.27×10^{-2}

Table 9
Predicted performance of both stacks in IT-SOFC CHP system at 50% rated electrical power output

Parameter	Stack 1	Stack 2
Stack external current (A)	12.0	12.0
Stack voltage (V)	107.3	107.5
Mean cell voltage (V)	0.789	0.790
Stack mean external current density (mA cm^{-2})	83.3	83.3
Stack mean power density (mW cm^{-2})	66	66
Stack centre temperature (°C)	579	587
Air inlet temperature (°C)	480	480
Fuel inlet temperature (°C)	641	641
Air outlet temperature (°C)	611	624
Fuel outlet temperature (°C)	612	625
Mean electronic leakage current (A)	2.4	3.3
Mean electronic leakage current density (mA cm^{-2})	16.7	22.9
Fuel flow rate (kg s^{-1})	2.66×10^{-4}	2.66×10^{-4}
Air flow rate (kg s^{-1})	8.13×10^{-3}	7.97×10^{-3}

Table 10
Predicted performance of heated steam reformer in IT-SOFC CHP system at 100% and 50% rated electrical power output

Parameter	100% Power	50% Power
Fuel inlet temperature (°C)	144	268
Reformate outlet temperature (°C)	630	641
Exhaust inlet temperature (°C)	882	834
Exhaust outlet temperature (°C)	692	682
Heat input from exhaust (W)	3394	1642
Exhaust mass flow rate (kg s^{-1})	1.403×10^{-2}	8.67×10^{-3}
Reformate mass flow rate (kg s^{-1})	1.1×10^{-3}	5.32×10^{-4}

cell and 70% fuel utilisation. It can also be seen that the predicted electronic leakage current is only around 4% of the total applied current, and therefore its effect on the cell efficiency is negligible. The small predicted difference in the performance of the two stacks relates to the small difference in air flow as some of the oxygen has been depleted by stack 1 before being fed to stack 2. This means that for the same air inlet temperature stack 2 is slightly less cooled, and therefore runs at a slightly higher temperature. An air temperature rise of around 150 K is predicted, which is typical for SOFC operation (Tables 9–12).

Table 9 shows the same stack data as Table 8, but at 50% power. The stack efficiency stays approximately constant as the load is reduced, as the increased efficiency as a result of the increased cell potential is offset by the increased electronic leakage current. Table 10 shows the predicted performance

Table 11
Predicted reformate composition from heated steam reformer in IT-SOFC CHP system at 100% and 50% rated electrical power output

Fuel component	100% Power (mol%)	50% Power (mol%)
Methane	3.5	2.7
Carbon monoxide	5.9	6.6
Hydrogen	51.1	52.5
Carbon dioxide	8.6	8.5
Steam	30.9	29.7

Table 12
Predicted performance of air blower C1 in IT-SOFC CHP system at 100% and 50% rated electrical power output

Parameter	100% Power	50% Power
Pressure rise (mbar)	229	136
Electrical power input (W)	726	275
Fan speed (rpm)	1860	1162
Outlet temperature (°C)	57	44

of the heated steam reformer at full and half load. The reformer performance is predicted to scale well, although as would be expected the internal heat exchange between the reformer and the hot exhaust stream becomes more efficient at part load as the mass flow of gas is smaller relative to the available heat exchange area. Related to this, Table 11 shows the predicted reformate composition at full and part load. Because the reformate temperature is predicted to be higher at part load the conversion is slightly higher, with less methane in the reformate, and the carbon monoxide concentration is slightly higher because of the change in the WGS equilibrium composition. Finally Table 12 shows the predicted performance of the air blower C1 at full and half power. The pressure drops of the system components were modelled as directly proportional to the mass flowrate, so at half power and approximately half the mass flowrate, the pressure rise required is approximately half that at full power.

6. Conclusions

It has been demonstrated that the unique metal-supported IT-SOFC cell concept developed by Ceres Power is capable of being incorporated into stacks and systems to deliver commercially competitive levels of efficiency and power density. In particular, it is demonstrated that the mixed conductivity inherent in the use of CGO electrolytes is not detrimental to efficiency under practical operating conditions. The modelling of stacks and a CHP system concept has been based upon present cell performance, and consequently no major technological improvements in the underlying fuel cell technology are required in order to achieve the performance levels predicted in this work. There is considerable scope for improving the cell performance to levels above that reported here, and indeed development cells capable of power densities in excess of 500 mW cm^{-2} have been demonstrated, indicating the scope to further improve both stack power density and system efficiency.

Acknowledgements

cussions, and for their contribution to the Ceres development programme.

References

[1] N.P. Brandon, D. Corcoran, D. Cummins, A. Duckett, K. El-Khoury, D. Haigh, R. Leah, G. Lewis, N. Maynard, T. McColm, R. Trezona, A. Selcuk, M. Schmidt, Development of metal supported solid oxide fuel cells for operation at 500–600 °C, J. Mater. Eng. Perform. 13 (3) (2004) 253–256.

[2] B.C.H. Steele, Materials for IT-SOFC stacks 35 years R&D: the inevitability of gradualness? Solid State Ionics 134 (2000) 3–20.

[3] P. Aguiar, C.S. Adjiman, N.P. Brandon, Anode-supported intermediate temperature direct internal reforming solid oxide fuel cell. I: model-based steady-state performance, J. Power Sources 138 (1–2) (2004) 120–136.

[4] P. Bance, N.P. Brandon, B. Girvan, P. Holbeche, S. O'Dea, B.C.H. Steele, Spinning out a fuel cell company from a UK university—two years of progress at Ceres Power, J. Power Sources 131 (1 and 2) (2004) 86–90.

[5] M. Sahibzada, R.A. Rudkin, B.C.H. Steele, I.S. Metcalfe, J.A. Kilner, in: U. Stimming, et al. (Eds.), SOFC V, Proceedings Volume, 97–40, Electrochemical Society, NJ, 1997, p. 244.

[6] S.H. Chan, K.A. Khor, Z.T. Xia, A complete polarization model of a solid oxide fuel cell and its sensitivity to the change of cell component thickness, J. Power Sources 93 (2001) 130–140.

[7] A.V. Virkar, J. Chen, C.W. Tanner, J. Kim, The role of electrode microstructure on activation and concentration polarizations in solid oxide fuel cells, Solid State Ionics 131 (2000) 189–198.

[8] J. Kim, A.V. Virkar, K. Fung, K. Mehta, S.C. Singhal, Polarization effects in intermediate temperature, anode-supported solid oxide fuel cells, J. Electrochem. Soc. 146 (1999) 69–78.

[9] B.C.H. Steele, Appraisal of $Ce_{1-y}Gd_yO_{2-y/2}$ electrolytes for IT-SOFC operation at 500 °C, Solid State Ionics 129 (2000) 95–110.

[10] I. Riess, Theoretical treatment of the transport equations for electrons and ions in a mixed conductor, J. Electrochem. Soc. 128 (1981) 2077–2081.

[11] Process Systems Enterprise Ltd., gPROMS 2.3.1 Introductory User Guide, London, 2004.